



Optical Observations of the Young Type Ic Supernova SN 2014L in M99

Jujia Zhang^{1,2,3,4}, Xiaofeng Wang⁵, József Vinkó^{6,7,8}, J. Craig Wheeler⁸, Liang Chang^{1,3,4}, Yi Yang^{2,9,12}, Lifan Wang², Qian Zhai^{1,3,4}, Liming Rui⁵, Jun Mo⁵, Tianmeng Zhang¹⁰, Yu Zhang¹¹, Jianguo Wang^{1,3,4}, Jirong Mao^{1,3,4}, Chuanjun Wang^{1,3,4}, Weimin Yi^{1,3,4}, Yuxin Xin^{1,3,4}, Wenxiong Li⁵, Baoli Lun^{1,3,4}, Kaixing Lu^{1,3,4}, Hanna Sai⁵, Xiangming Zheng^{1,3,4}, Xiliang Zhang^{1,3,4}, Xu Zhou¹⁰, and Jinming Bai^{1,3,4}

¹ Yunnan Observatories (YNAO), Chinese Academy of Sciences, Kunming 650216, People's Republic of China; jujia@ynao.ac.cn

² George P. and Cynthia Woods Mitchell Institute for Fundamental Physics & Astronomy, Texas A. & M. University, College Station, TX 77843, USA

³ Key Laboratory for the Structure and Evolution of Celestial Objects, Chinese Academy of Sciences, Kunming 650216, People's Republic of China

⁴ Center for Astronomical Mega-Science, Chinese Academy of Sciences, 20A Datun Road, Chaoyang District, Beijing, 100012, People's Republic of China

⁵ Physics Department and Tsinghua Center for Astrophysics (THCA), Tsinghua University, Beijing 100084, People's Republic of China

⁶ Konkoly Observatory, Research Centre for Astronomy and Earth Sciences, Konkoly Thege ut 15-17, Budapest, 1121, Hungary

⁷ Department of Optics and Quantum Electronics, University of Szeged, H-6720 Szeged, Dómtér 9., Hungary

⁸ Department of Astronomy, University of Texas at Austin, Austin, TX 78712-1205, USA

⁹ Department of Particle Physics and Astrophysics, Weizmann Institute of Science, Rehovot 76100, Israel

¹⁰ National Astronomical Observatories of China (NAOC), Chinese Academy of Sciences, Beijing 100012, People's Republic of China

¹¹ Xinjiang Astronomical Observatory(XAO), Chinese Academy of Sciences, Urumqi, 830011, People's Republic of China

Received 2017 November 12; revised 2018 April 19; accepted 2018 June 20; published 2018 August 14

Abstract

We present optical spectroscopic and photometric observations of the nearby type Ic supernova (SN Ic) SN 2014L. This SN was discovered by the Tsinghua-NAOC Transient Survey (TNTS) in the nearby type-Sc spiral galaxy M99 (NGC 4254). Fitting to the early-time light curve indicates that SN 2014L was detected at only a few hours after the shock breakout, and it reached a peak brightness of $M_V = -17.73 \pm 0.28$ mag ($L = [2.06 \pm 0.50] \times 10^{42}$ erg s⁻¹) approximately 13 days later. SN 2014L shows a close resemblance to SN 2007gr in the photometric evolution, while it shows stronger absorption features of intermediate-mass elements (especially Ca II) in the early-time spectra. Based on simple modeling of the observed light curves, we derived the mass of synthesized ⁵⁶Ni as $M_{\text{Ni}} = 0.075 \pm 0.025 M_{\odot}$, and the mass and total energy of the ejecta as $M_{\text{ej}} = 1.00 \pm 0.20 M_{\odot}$ and $E_{\text{ej}} = 1.45 \pm 0.25$ foe, respectively. Given these typical explosion parameters, the early detection, and the extensive observations, we suggest that SN 2014L could be a template sample for the investigation of SNe Ic.

Key words: supernovae: individual (SN 2014L)

Supporting material: data behind figure, machine-readable tables

1. Introduction

Type Ic supernovae are characterized by the absence of hydrogen and helium in the spectra (see, e.g., reviews by Filippenko 1997; Modjaz et al. 2014; Liu et al. 2016; Branch & Wheeler 2017). The primary spectral distinction between regular Ic and Ib is the strength and evolution of helium lines. Recent studies show, however, that weak helium absorptions can be detected in some SNe Ic (Chen et al. 2014; Milisavljevic et al. 2015), while there are also arguments that the helium features are not present in SNe Ic (i.e., Liu et al. 2016). Theoretically, the appearance of helium in the spectra may not necessarily suggest a classification of an SN Ib, which might relate to the abundance ratio of nickel and helium in the outer layers (Wheeler et al. 1987; Shigeyama et al. 1990; Hachisu et al. 1991).

Observationally, SNe Ic are found to show large varieties in spectral features and line profiles. For example, the subclass of broad-lined SNe Ic (BL-Ic) are characterized by broad, highly blueshifted line profiles in their spectra, relatively high luminosity, and considerable kinetic energies of $(2-5) \times 10^{52}$ erg (Woosley & Bloom 2006). Some BL SNe Ic are found to be associated with long-duration gamma-ray bursts (GRBs), e.g., SN 1998bw (Galama et al. 1998; Iwamoto et al. 1998) and SN 2003dh (Hjorth et al. 2003;

Mazzali et al. 2003), and their progenitors are reported to have relatively low metallicity (e.g., Woosley et al. 1993; Woosley & Bloom 2006). On the other hand, there are some peculiar SNe Ic events with prominent calcium features and fast spectral evolution, i.e., SN 2012hn (Valenti et al. 2014), which are dubbed as Ca-rich SNe Ic. This observed diversity of SNe Ic indicates that they may arise in different channels, e.g., single massive stars or binary system.

Photometric and spectroscopic observations have been published for dozens of SNe Ic (Bianco et al. 2014; Modjaz et al. 2014). However, the sample with very early observations and good phase coverage (e.g., SN 1994I, Wheeler et al. 1994; Filippenko et al. 1995; Richmo et al. 1996; SN 2007gr, Valenti et al. 2008; Hunter et al. 2009; Chen et al. 2014; SN 2013ge, Drout et al. 2016) is still limited. In this paper, we present the extensive photometric and spectroscopic observations of the nearby SN Ic SN 2014L, spanning from ~ -10 days to ~ 140 days relative to the maximum light. This SN was detected at only a few hours after the shock breakout and might be one of the youngest SN Ic ever discovered.

This paper is organized as follows. Observation and data reductions are described in Section 2. The results from photometry and spectroscopy are presented in Sections 3 and 4, respectively. Explosion parameters are calculated and discussed in Section 5. A summary is given in Section 6.

¹² Benozio Fellow.

2. Observations

SN 2014L was discovered by the Tsinghua—NAOC (National astronomical observatories of China) transient survey (TNTS) on 2014 January 26.83 UT (Zhang et al. 2014b) in the nearby Sc-type galaxy M99 (=NGC 4254), at an unfiltered magnitude of 17.2. This survey uses a 0.6 m Schmidt telescope (+4K × 4K CCD) located at Xinglong Observatory in China (Zhang et al. 2015). K. Itagaki reported a pre-discovery detection of this transient (with an unfiltered magnitude of 17.9), obtained on 2014 January 24.85 UT with a 0.5 m reflector at the Takamizawa station, Japan. The coordinates of this transient is R.A. = 12^h18^m48^s.68 and decl. = +14°24′43″.5 (J2000), locating at 13″.8 west and 15″.9 south of the center of the host galaxy. The latest distance measurement of M99 reported by Tully et al. (2013) as 13.9 ± 1.5 Mpc based on the Tully–Fisher relation is adopted in this paper. This result well matches an alternative distance reported by Poznanski et al. (2009) as 14.4 ± 2.0 Mpc via the expanding photosphere method.

SN 2014L was independently classified as a young SN Ic by several groups (e.g., Akitaya et al. 2014; Li et al. 2014; Ochner et al. 2014; Zhang & Wang 2014) within 1–2 days after the discovery. We thus triggered the follow-up observation campaign on the Li-Jiang 2.4 m telescope (LJT; Fan et al. 2015) with YFOSC (Yunnan Faint Object Spectrograph and Camera; Zhang et al. 2014a) at Li-Jiang Observatory of Yunnan Observatories (YNAO) and the Tsinghua-NAOC 0.8 m telescope (TNT; Wang et al. 2008; Huang et al. 2012) at Xing-Long Observatory NAOC. This campaign spans from $t \approx -10$ days to $t \approx +140$ days, or from $\tau \approx +3$ days to $\tau \approx +150$ days (parameter t denotes to the time relative to the V -band maximum, τ denotes to the time compared to the shock breakout in this paper) covering the full photospheric phase. The daily observations at the first month after shock breakout makes SN 2014L an excellent object for studying the observed properties of SNe Ic.

Figure 1 shows the finder chart and the pre-discovery images of SN 2014L taken by the *HST* Wide-Field Planetary Camera 2 (WFPC2) on Jan, 2009 under *HST* program GO-11966 (PI: Regan). At the distance of $D = 13.9 \pm 1.5$ Mpc, the corresponding physical pixel size in the sky is $d \sim 7$ pc per pixel. In these pre-explosion images, no point-like source can be detected within 0″.2 from the SN position. The apparent brightness of the white circle region is estimated as $m_{F336W} = 22.3 \pm 4.0$ mag, $m_{F606W} = 21.1 \pm 0.5$ mag and $m_{F814W} = 20.5 \pm 0.6$ mag. On the other hand, there are some brighter and bluer sources located not far from the SN position (i.e., $\sim 0″.6$). Given the high star formation rate of M99 (Soria & Wong 2016), the nearby blue sources around the birth place, the larger host extinction of SN 2014L (see the details in Section 3.2), and the strong Balmer emission lines presented in the spectra (see the details in Section 2.2), SN 2014L likely comes from a relatively young stellar environment covered by thick dust and gas.

2.1. Photometry

SN 2014L is well-observed in the standard Johnson UBV and Kron–Cousins RI bands, with a typical FWHM 1″.6 for LJT images, and 2″.5 for the TNT images. High-quality template images were taken with the LJT+YFOSC and TNT at 2–3 years after the explosion. We perform background subtraction to remove the time-invariant background structures and better reveal

the time-variant SN signals. The photometry of this SN is transformed into the standard Johnson–Cousin photometry system (as listed in Table 1 and presented in Figure 2) through some local standard stars, as marked in the left panel of Figure 1. The $UBVRI$ magnitudes of these reference stars (as listed in Table 2) are calibrated via observing a series of Landolt (1992) photometric standard stars on three photometric nights.

2.2. Spectroscopy

Figure 3 shows the spectral sequence of SN 2014L over a period of about four months starting from 2014 January 27. The observation journal of these spectra is listed in Table 3, including 13 spectra from the LJT (+YFOSC) and 1 spectrum from the Xing-Long 2.16 m telescope (XLT) with the BFOSC (Beijing Faint Object Spectrograph and Camera). All of these spectra are calibrated in both wavelength and flux, and they are corrected for telluric absorption and redshift. The narrow emission lines (e.g., $H\alpha$, $H\beta$) presented in the spectra are due to the contamination in the host galaxy, which becomes dominating at late phase. Variations of these narrow emissions are due to the slit position and spectral resolution. Two spectra from the ANU WiFeS SuperNova Program (AWSNAP; Childress et al. 2016) are also included in this figure to fill the observation gaps.

3. Photometric Results

A polynomial fit is applied to the $UBVRI$ band light curves around the maximum light to derive the peak magnitudes, dates, and the post-peak decline rates, as listed in Table 4. For example, SN 2014L reached its V -band peak on MJD = 56694.81, and it reached the peaks at slightly different epochs in other bands. By adopting the distance $D = 13.9 \pm 1.5$ Mpc (as discussed in Section 2) and the total extinction $E(B - V) = 0.67 \pm 0.11$ (derived in Section 3.2), we obtain an absolute V -band peak magnitude of -17.73 ± 0.28 mag for SN 2014L.

3.1. Light Curves

Figure 4 displays the $UBVRI$ light curves of SN 2014L compared to those of some typical SNe to better understand the photometric properties of SN 2014L. Three SNe Ic, SN 1994I (Richmo et al. 1996), SN 2007gr (Valenti et al. 2008; Chen et al. 2014), and SN 2004aw (Taubenberger et al. 2006); the board-line SN Ic, SN 1998bw (Clocchiatti et al. 2011); SN Ib, SN 2008D (Modjaz et al. 2009; Tanaka et al. 2009; Bianco et al. 2014); faint and calcium-rich events SN 2005E (Perets et al. 2010) and SN 2012hn (Valenti et al. 2014) are plotted in Figure 4.

The light curves of SN 2014L are overall similar to those of SN 2007gr, though the former appears slightly narrower than the latter. It is surprising that SN 2014L, SN 2004aw, SN 2007gr, and SN 1998bw show similar evolution in the U band, with a small scatter of < 0.2 mag. In the B band, SN 2014L, SN 1994I and SN 2012hn also show similar light-curve evolution at $t < +20$ days. After that, these SNe exhibit different decay rates. Larger scatters also exist in the VRI bands at similar phases.

These SNe can be divided into three clusters, depending on the decline rate from $0 < t < +30$ days. For example, the slow declining group including SN 2004aw, SN BL-Ic 1998bw, SN Ib 2008D; the fast declining group including SN Ic 1994I and SN Ca-rich 2005E; and the intermediate declining group

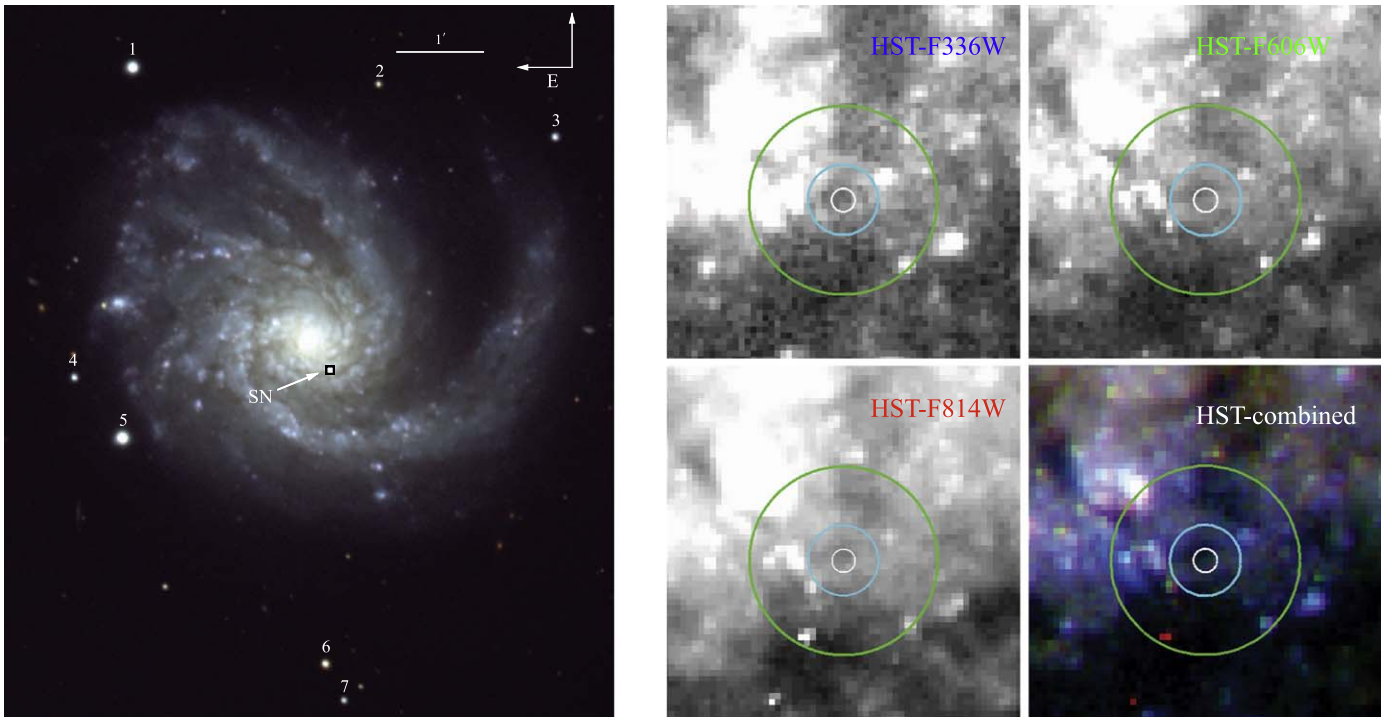


Figure 1. Left panel: the finder chart of SN 2014L and its local reference, taken by the LJT and YFOSC on 2014 January. The mean FWHM of this combined image is $1''/60$ under the scale of $0''/28/\text{pixel}$. Right panel: the pre-explosion image, corresponding to the black box on the left panel and including the birth place region of SN 2014L, taken by *Hubble Space telescope* Wide-Field Planetary Camera 2 in 2009 in the filters of F336W, F606W, and F814W under the scale of $0''/1/\text{pixel}$. The combined image is also shown. The circles having radii of $0''/2$, $0''/6$ and $1''/6$, respectively, are centered at the location of SN.

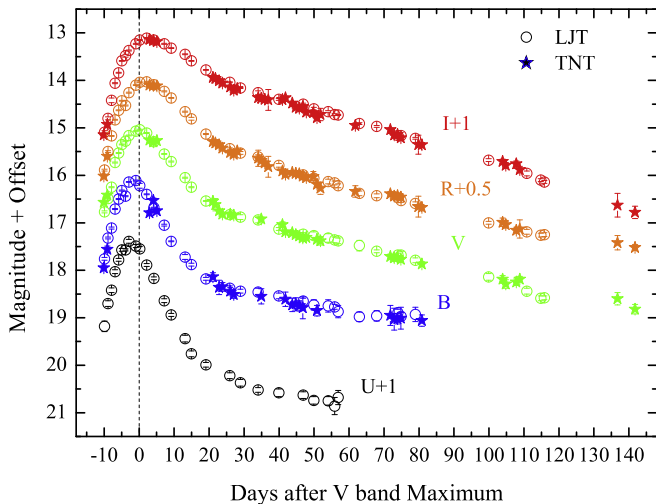


Figure 2. *UBVRI* light curves of SN 2014L obtained at the Li-Jiang 2.4 m telescope and *BVRI* light curves obtained at the Tsinghua-NAOC 0.8 m telescope. An offset has been added for better visibility.

including SN Ic 2014L, SN Ic 2007gr, and SN Ca-rich 2012hn. In each cluster, however, apparent differences can be found in spectral comparisons at both photospheric and nebular phase of Section 4.

The relatively similar peak properties are often in contrast with the considerable spread in the properties of the late-time tail of the light curve (e.g., Wheeler et al. 2015, hereafter is WJC 15). Clear differences existing among the tails of these light curves might be related to the different optical opacities and γ -ray leakage rates of different SNe Ib/c.

3.2. Reddening

The early spectra of SN 2014L show red continuum and significant absorption of narrow NaID from the host galaxy. These features suggest substantial line-of-sight reddening towards the SN. The equivalent width (EW) of NaID absorption in the SN spectra can be used to estimate the reddening according to some empirical correlations between reddening and EW of NaID, e.g., $E(B - V) = 0.16 \text{EW}_{\text{Na}} - 0.01$ (Turatto et al. 2003), and $E(B - V) = 0.25 \text{EW}_{\text{Na}}$ (Barbon et al. 1990). However, these empirical correlations usually exhibit large scatter for the extinction measurement (e.g., Poznanski et al. 2011; Phillips et al. 2013). In SN 2014L, $\text{EW}(\text{Na I D})$ is measured as $2.7 \pm 0.1 \text{ \AA}$, which corresponds to a color excess of $E(B - V)_{\text{host}} = 0.42 \pm 0.04$ or 0.68 ± 0.05 following the above relations.

Alternatively, the host-galaxy reddening of SNe Ib/c can be estimated by a photometric method. Based on a larger sample of SNe Ib/c, Drout et al. (2011) found that the $V - R$ color of extinction-corrected SNe Ib/c is tightly clustered at 0.26 ± 0.06 mag at $t \approx +10$ days after the V -band maximum, and 0.29 ± 0.08 mag at $t \approx +10$ days after the R -band maximum. This method yields an estimate of $E(B - V)_{\text{total}} = 0.75 \pm 0.05$ mag for SN 2014L assuming an $R_V = 3.1$ Milky Way extinction law for the host galaxy. Adopting the Galactic extinction $E(B - V)_{\text{Gal}} = 0.04 \pm 0.01$ (Schlafly & Finkbeiner 2011), the host reddening derived from the $V - R$ color is $E(B - V)_{\text{host}} = 0.71 \pm 0.05$ mag.

Combining the estimations obtained from NaID absorption and $V - R$ color, an average value of the total reddening, $E(B - V) = 0.67 \pm 0.11$ mag, is adopted in this paper.

Table 1
UBVRI band Photometry of SN 2014L

Date	MJD	Day ^a	<i>U</i> (mag)	<i>B</i> (mag)	<i>V</i> (mag)	<i>R</i> (mag)	<i>I</i> (mag)	Telescope
Jan 27	56684.72	-10.09	...	17.95(0.06)	16.57(0.02)	16.52(0.03)	16.15(0.03)	TNT
Jan 27	56684.90	-9.91	18.18(0.11)	17.76(0.03)	16.77(0.02)	16.39(0.02)	16.09(0.03)	LJT
Jan 28	56685.74	-9.07	...	17.56(0.07)	16.42(0.02)	16.10(0.03)	15.93(0.03)	TNT
Jan 28	56685.91	-8.90	17.70(0.06)	17.32(0.02)	16.49(0.01)	16.00(0.02)	15.80(0.03)	LJT
Jan 29	56686.92	-7.89	17.42(0.05)	17.11(0.02)	16.25(0.01)	15.67(0.01)	15.42(0.05)	LJT
Jan 30	56687.90	-6.91	17.03(0.04)	16.71(0.01)	15.73(0.01)	15.33(0.01)	15.06(0.01)	LJT
Jan 31	56688.95	-5.86	16.78(0.03)	16.50(0.01)	15.53(0.01)	15.13(0.01)	14.84(0.01)	LJT
Feb 01	56689.89	-4.92	16.57(0.03)	16.32(0.01)	15.35(0.01)	14.93(0.01)	14.59(0.01)	LJT
Feb 02	56690.94	-3.87	16.57(0.02)	16.44(0.01)	15.28(0.01)	15.03(0.01)	14.48(0.03)	LJT
Feb 03	56691.87	-2.94	16.39(0.04)	16.14(0.01)	15.16(0.01)	14.76(0.01)	14.37(0.01)	LJT
Feb 05	56693.90	-0.91	16.49(0.03)	16.11(0.01)	15.07(0.01)	14.60(0.01)	14.23(0.01)	LJT
Feb 06	56694.95	0.14	16.55(0.05)	16.22(0.05)	15.04(0.01)	14.54(0.01)	14.15(0.01)	LJT
Feb 08	56696.96	2.15	16.89(0.03)	16.40(0.01)	15.11(0.01)	14.53(0.01)	14.11(0.01)	LJT
Feb 09	56697.79	2.98	...	16.79(0.05)	15.26(0.01)	14.60(0.02)	14.14(0.02)	TNT
Feb 10	56698.87	4.06	...	16.53(0.05)	15.30(0.01)	14.61(0.02)	14.16(0.02)	TNT
Feb 11	56699.01	4.20	17.17(0.03)	16.68(0.01)	15.29(0.01)	14.59(0.01)	14.15(0.01)	LJT
Feb 11	56699.87	5.06	...	16.75(0.05)	15.27(0.01)	14.62(0.02)	14.19(0.02)	TNT
Feb 14	56702.00	7.19	17.64(0.04)	17.05(0.02)	15.55(0.01)	14.73(0.01)	14.23(0.01)	LJT
Feb 15	56703.99	9.18	17.94(0.03)	17.39(0.01)	15.71(0.01)	14.87(0.01)	14.32(0.01)	LJT
Feb 19	56707.94	13.13	18.44(0.07)	17.72(0.05)	16.05(0.01)	15.16(0.01)	14.45(0.01)	LJT
Feb 21	56709.75	14.94	18.76(0.06)	17.88(0.03)	16.25(0.01)	15.31(0.03)	14.59(0.01)	LJT
Feb 25	56713.89	19.08	18.99(0.05)	18.18(0.03)	16.54(0.01)	15.63(0.01)	14.78(0.01)	LJT
Feb 02	56715.89	21.08	...	18.14(0.09)	16.55(0.02)	15.79(0.03)	14.94(0.02)	TNT
Feb 28	56716.64	21.83	16.62(0.13)	15.82(0.05)	14.96(0.04)	TNT
Mar 01	56717.65	22.84	...	18.36(0.15)	16.75(0.03)	15.86(0.04)	15.01(0.03)	TNT
Mar 02	56718.62	23.81	...	18.35(0.09)	16.82(0.02)	15.93(0.03)	15.06(0.03)	TNT
Mar 04	56720.72	25.91	19.22(0.06)	18.38(0.05)	16.83(0.02)	15.94(0.02)	15.04(0.01)	LJT
Mar 04	56720.87	26.06	...	18.44(0.08)	16.82(0.03)	16.02(0.03)	15.14(0.02)	TNT
Mar 05	56721.85	27.04	...	18.51(0.08)	16.84(0.02)	16.06(0.02)	15.21(0.02)	TNT
Mar 06	56722.85	28.04	15.99(0.04)	15.18(0.03)	TNT
Mar 07	56723.79	28.98	19.37(0.07)	18.44(0.04)	16.88(0.05)	16.03(0.03)	15.16(0.01)	LJT
Mar 12	56728.84	34.03	19.52(0.05)	18.46(0.08)	16.94(0.06)	16.11(0.04)	15.26(0.04)	LJT
Mar 12	56728.85	34.04	16.14(0.17)	15.36(0.04)	TNT
Mar 13	56729.71	34.90	...	18.55(0.16)	16.92(0.04)	16.19(0.04)	15.38(0.04)	TNT
Mar 14	56730.71	35.90	16.24(0.06)	15.40(0.03)	TNT
Mar 15	56731.71	36.90	16.32(0.22)	15.41(0.22)	TNT
Mar 18	56734.75	39.94	19.58(0.08)	18.54(0.06)	17.13(0.03)	16.29(0.04)	15.40(0.02)	LJT
Mar 19	56735.76	40.95	17.04(0.06)	16.41(0.04)	15.41(0.03)	TNT
Mar 20	56736.65	41.84	...	18.61(0.15)	17.19(0.03)	16.48(0.05)	15.37(0.03)	TNT
Mar 22	56738.61	43.80	...	18.73(0.14)	17.21(0.02)	16.44(0.04)	15.48(0.03)	TNT
Mar 23	56739.62	44.81	...	18.71(0.13)	17.25(0.04)	16.46(0.04)	15.57(0.03)	TNT
Mar 24	56740.62	45.81	...	18.75(0.11)	17.28(0.04)	16.47(0.04)	15.59(0.03)	TNT
Mar 25	56741.62	46.81	...	18.79(0.23)	17.32(0.04)	16.52(0.07)	15.55(0.04)	TNT
Mar 25	56741.69	46.88	19.63(0.07)	18.65(0.06)	17.24(0.03)	16.49(0.02)	15.50(0.02)	LJT
Mar 26	56742.62	47.81	17.31(0.05)	16.55(0.05)	15.67(0.03)	TNT
Mar 28	56744.62	49.81	16.53(0.11)	15.68(0.06)	TNT
Mar 28	56744.76	49.95	19.74(0.08)	18.73(0.11)	17.27(0.08)	16.56(0.05)	15.60(0.03)	LJT
Mar 29	56745.63	50.82	...	18.85(0.11)	17.35(0.03)	16.69(0.04)	15.79(0.04)	TNT
Mar 30	56746.64	51.83	17.38(0.09)	16.77(0.13)	15.72(0.13)	TNT
Apr 01	56748.84	54.03	19.75(0.09)	18.75(0.13)	17.32(0.09)	16.63(0.05)	15.66(0.02)	LJT
Apr 03	56750.71	55.90	19.86(0.18)	18.77(0.05)	17.36(0.06)	16.66(0.04)	15.72(0.02)	LJT
Apr 04	56751.72	56.91	19.68(0.15)	18.87(0.13)	17.38(0.06)	16.72(0.04)	15.73(0.01)	LJT
Apr 09	56756.63	61.82	16.84(0.12)	15.95(0.05)	TNT
Apr 10	56757.78	62.97	...	18.98(0.10)	17.48(0.11)	16.88(0.05)	15.91(0.02)	LJT
Apr 15	56762.72	67.91	...	18.96(0.11)	17.60(0.03)	16.93(0.04)	15.97(0.02)	LJT
Apr 19	56766.63	71.82	...	18.95(0.21)	17.71(0.05)	16.89(0.05)	16.04(0.03)	TNT
Apr 20	56767.72	72.91	...	19.03(0.23)	17.74(0.06)	16.94(0.06)	16.15(0.05)	TNT
Apr 21	56768.69	73.88	...	19.02(0.11)	17.73(0.04)	16.93(0.04)	16.14(0.05)	TNT
Apr 21	56768.75	73.94	...	18.89(0.07)	17.68(0.04)	16.97(0.03)	16.16(0.04)	LJT
Apr 22	56769.65	74.84	...	19.01(0.23)	17.77(0.06)	16.96(0.06)	16.21(0.04)	TNT
Apr 22	56769.70	74.89	...	18.97(0.08)	17.68(0.07)	17.03(0.04)	16.16(0.01)	LJT
Apr 26	56773.77	78.96	...	18.93(0.15)	17.79(0.05)	17.09(0.03)	16.22(0.02)	LJT
Apr 27	56774.65	79.84	17.16(0.22)	16.36(0.20)	TNT
Apr 28	56775.65	80.84	...	19.06(0.12)	17.87(0.05)	17.18(0.05)	16.36(0.05)	TNT

Table 1
(Continued)

Date	MJD	Day ^a	U(mag)	B(mag)	V(mag)	R(mag)	I(mag)	Telescope
May 17	56794.72	99.91	18.14(0.07)	17.50(0.03)	16.68(0.03)	LJT
May 20	56798.70	103.89	18.19(0.08)	17.49(0.09)	16.71(0.05)	TNT
May 22	56799.61	104.80	18.29(0.09)	17.54(0.07)	16.79(0.06)	TNT
May 25	56802.64	107.83	18.25(0.07)	17.66(0.05)	16.76(0.06)	TNT
May 26	56803.64	108.83	18.19(0.06)	17.63(0.19)	16.88(0.07)	TNT
May 28	56805.63	110.82	18.44(0.06)	17.69(0.05)	16.96(0.05)	LJT
Jun 01	56809.62	114.81	18.59(0.05)	17.76(0.04)	17.10(0.03)	LJT
Jun 02	56810.65	115.84	18.58(0.04)	17.75(0.04)	17.14(0.03)	LJT
Jun 23	56831.57	136.76	18.60(0.13)	17.92(0.15)	17.63(0.25)	TNT
Jun 27	56836.57	141.76	18.82(0.10)	18.02(0.06)	17.78(0.13)	TNT

Notes.^a Relative to the V-band maximum, MJD = 56694.81.

(This table is available in machine-readable form.)

3.3. Color Curves

The reddening-corrected color curves of SN 2014L are displayed in Figure 5, together with those of the comparison sample shown in Figure 4. The $B - V$ color of SN 2014L is similar to that of SN 1998bw, SN 2008D, and SN 2007gr, but the difference exists in other bands, especially at $t > +20$ days relative to the V-band maximum. The scatter shown before the peak can be attributed to the difference in temperature and metal abundance of the outer ejecta, while the scatter seen after $t \approx +20$ days could be related to the duration of photospheric phase.

The large scatter among the colors of these SNe, even in the SNe Ib/c group, might not suggest a uniform color evolution for these SNe. However, as mentioned before, there seems to exist an intrinsic $V - R$ color for regular SNe Ib/c at about ten days after the peak (Drout et al. 2011). Such an inherent color distribution might also exist in $B - V$ and $V - I$ color at a similar phase in Figure 4.

3.4. Quasi-bolometric Light Curve

Figure 6 displays the quasi-bolometric light curves of our sample, based on the $UBVRI$ photometry presented in Figure 4. SN 2014L reaches the peak quasi-bolometric luminosity of $L = (2.06 \pm 0.50) \times 10^{42} \text{ erg s}^{-1}$ at MJD = 56693.86, which is about one day earlier than the V-band maximum. The fractional contribution of the ultraviolet (UV) and near-infrared (NIR) emission to the bolometric luminosity can be $\sim 30\%$ – 40% at around the peak for SNe Ib/c (e.g., $\sim 40\%$ in SN 2008D; Modjaz et al. 2009). Considering the missed UV and NIR flux of SN 2014L, the total bolometric flux of this SN could reach $\sim 3 \times 10^{42} \text{ erg s}^{-1}$ around the peak.

4. Spectral Evolution

The spectral sequence of SN 2014L, covering the full evolution at the photospheric and a part of the early nebular phase, was exhibited in Figure 3. A closer comparison between SN 2014L and other representative SNe Ib/c are presented at four selected phases as plotted in Figure 7. All of these spectra have been corrected for redshifts and reddening.

4.1. Early Phase

The early-time spectra (i.e., at a few days after the explosion) contain prominent features to distinguish it among different subclasses of SNe. Figure 7(a) shows the $t \sim -7$ day spectra of SN 2014L and some comparison SNe Ib/c including SN 2007gr (Chen et al. 2014), SN 1994I (Filippenko et al. 1995), SN 2004aw (Modjaz et al. 2014), SN 1998bw (Patat et al. 2001), and SN 2008D (Modjaz et al. 2009). Compared to the almost featureless spectrum of SN 2004aw and the board-lined spectrum of SN 1998bw, the spectra of SN 2014L, SN 2007gr, and SN 1994I are characterized by the absorptions of some intermediate-mass elements (IMEs, e.g., Ca, Si, O, and C) and Fe II. The clear absorption near 6150 \AA in the spectra of SN 2014L, SN 2007gr, and SN 1994I can be identified as the feature of Si II $\lambda 6355$. The absorption near about 5600 \AA is likely attributed to the absorption of Na I D rather than He I $\lambda 5876$ because of the absence of other helium lines as found in the spectrum of SN Ib 2008D. Overall, SN 2014L shows close resemblances to SN 2007gr and SN 1994I, except that it has more prominent absorption features of Ca II NIR triplet. The difference in absorptions of Ca II NIR triplet might indicate difference at the outer layer of ejecta, as discussed in Section 4.5.

4.2. Around Maximum

At around the maximum, the spectral features of SN 2014L are very similar to those of SN 2007gr. These two SNe Ic show narrower absorptions of Si, O, Na, and Fe than SN 1994I and SN 2004aw. In particular, SN 2014L seems to have unusually strong absorption features for a Ca II NIR triplet, comparable to that of the Ca-rich events such as SN 2005E (Perets et al. 2010) and SN 2012hn (Valenti et al. 2014). The strong Ca II NIR triplet in SN 2014L might relate to the abundance enrichment of IMEs at the outer layer. To investigate the relative abundance of Si, Ca, and O measured from the spectra shown in Figure 7(b), we plot the EW ratio of O I $\lambda 7774$ /Ca II NIR triplet versus Si II $\lambda 6355$ /Ca II NIR triplet in Figure 8. One can see that the absorption lines ratio Ca/O of SN 2014L is close to that of SN 1994I, while the Ca/Si ratio of SN 2014L is similar to that of SN 2007gr. Both of these two ratios measured from SN 2014L are smaller than the calcium-rich events like SN 2005E and SN 2012hn, ruling out the calcium-rich subclass. Nevertheless, the synthetic spectra at around maximum by

Table 2
The *UBVRI* band Magnitudes of the Local Photometric Standards in the Field of SN 2014L

Star	<i>U</i> (mag)	<i>B</i> (mag)	<i>V</i> (mag)	<i>R</i> (mag)	<i>I</i> (mag)
1	15.05(0.02)	14.74(0.01)	14.01(0.02)	13.62(0.01)	13.24(0.02)
2	19.61(0.04)	18.56(0.01)	17.46(0.02)	16.78(0.02)	16.17(0.03)
3	17.29(0.03)	17.28(0.02)	16.67(0.01)	16.33(0.02)	15.96(0.02)
4	17.51(0.03)	17.47(0.02)	16.78(0.01)	16.41(0.01)	16.02(0.02)
5	14.30(0.02)	14.11(0.01)	13.44(0.01)	13.09(0.02)	12.73(0.02)
6	19.03(0.03)	17.60(0.01)	16.28(0.01)	15.46(0.01)	14.72(0.01)
7	18.36(0.03)	18.23(0.01)	17.39(0.02)	16.93(0.01)	16.44(0.02)

Note. See Figure 1 for the finder chart of these reference stars.

(This table is available in machine-readable form.)

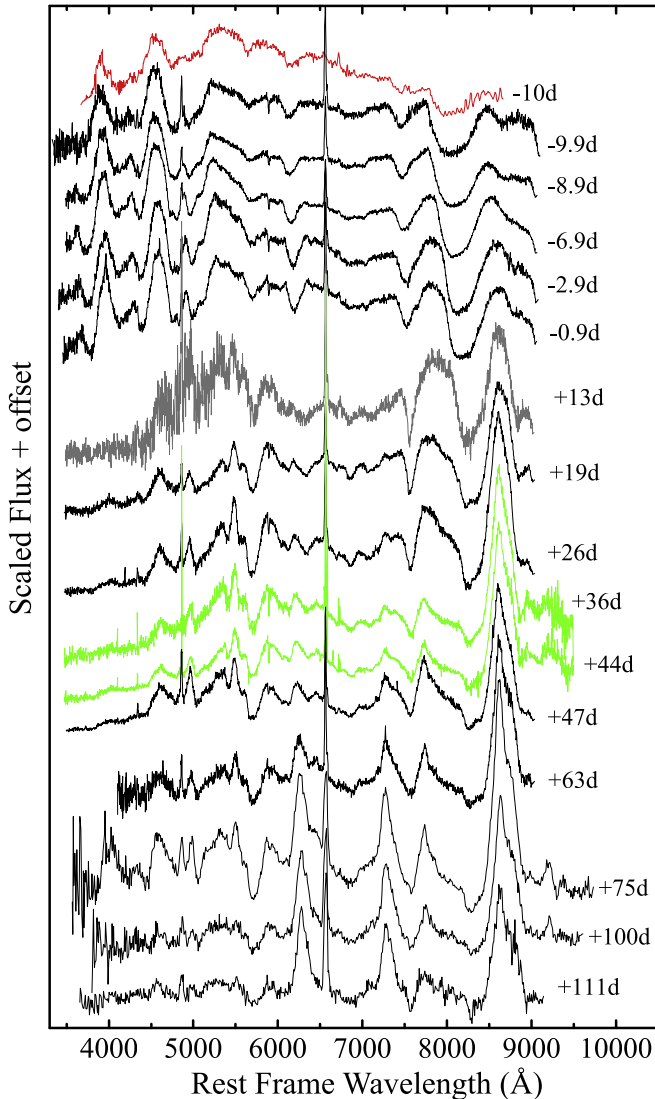


Figure 3. Spectral series of SN 2014L. The black spectra are from the Li-Jiang 2.4 m telescope, the red one is from the Xi-Long 2.16 m telescope, and the green are from the ANU WiFeS SuperNova Program. The data used to create this figure are available.

(Iwamoto et al. 1998) suggests that the strength of Ca II NIR triplet is weaker than that of Si II and O I.

Compared to other subclasses of SNe Ib/c, the BL SNe Ic tend to cluster at the top right region of Figure 8. Note, however, that it is hard to measure the absorptions of Ca II NIR

triplet and O I $\lambda 7774$ in the spectra of SN 1998bw because these two features are blended before and near the maximum light. Moreover, these absorptions cover the wavelength range of the high-velocity Ca II NIR triplet and the photospheric components of Ca II NIR triplet and O I $\lambda 7774$.

According to the distributions shown in Figures 8 and 6, we can divide our sample of SNe Ib/c into three groups. For example, SN 2005E and SN 2012hn had lower luminosity and are located at the bottom of Figure 8. The SN 1998bw-like objects tend to have a smaller amount of calcium and higher luminosity, while the remaining SNe Ib/c in our sample have a moderate luminosity and lie in the center of Figure 8. Of the selected sample, SN 2004aw can be regarded as the transitional event linking the BL SNe Ic with the ordinary ones. The distribution of SNe Ic in Figures 8 and 6 suggests that the relative strength of Ca II NIR triplet measured in the near-maximum spectra is inversely related to their peak luminosities. Namely, SNe Ic with a significant amount of calcium tend to have lower luminosities. This result may still suffer from small-number statistics, but it is consistent with the theoretical prediction that the O/Ca ratio increases with the mass of progenitor for core-collapse SNe (Houck & Fransson 1996). Thus, a comparable O/Ca ratio seen in SN 2014L, SN 1994I, and SN 2007gr might imply that they have similar progenitor masses and brightness, while SN 2004aw and SN 1998bw are likely from more massive progenitors. It is possible that the Ca-rich events might have lower-mass progenitor systems given the fact that they tend to occur at positions far from the host galaxies. However, massive stars could go for an outing through tidal stripping during galaxy interactions. And we can not rule out a massive progenitor scenario for the Ca-rich events thoroughly (Kasliwal et al. 2012).

4.3. One Month after Maximum

By $t \sim 1$ month, the spectra show a clear distinction for different SNe Ic, as shown in Figure 7(c). For example, the $t \approx +26$ day spectrum of SN 2014L shows a close resemblance to the $t \approx +35$ day of SN 2007gr and the $t \approx +26$ day spectrum of SN 1994I, while its $t \approx +36$ day spectrum shows less photospheric features compared to the $t \approx +35$ day spectrum of SN 2007gr. This implies that SN 2014L has a relatively faster spectral evolution than SN 2007gr. In comparison, the Ca-rich class seems to be the most rapidly evolving spectral feature. At this phase, some nebular features, such as the emission at around 7300 Å (due to the blended lines of O II and Ca II) started to emerge. The significant differences in the spectral evolution conform to the scatter seen in the color curves at similar phases. This carbon feature becomes unambiguous in

Table 3
Journal of Spectroscopic Observations of SN 2014L

Date (UT)	MJD	Epoch ^a (days)	Res. (Å)	Range (Å)	Exp. Time (s)	Airmass	Telescope (+Instrument)
Jan 27	56684.81	-10.00	3700-8700	16	3000	1.13	XLT+BFOSC
Jan 27	56684.91	-9.90	3380-9150	18	2100	1.04	LJT+YFOSC
Jan 28	56685.91	-8.90	3520-9130	18	2400	1.04	LJT+YFOSC
Jan 30	56687.91	-6.90	3520-9130	18	2100	1.04	LJT+YFOSC
Feb 03	56691.88	-2.93	3430-9150	18	1800	1.03	LJT+YFOSC
Feb 05	56693.90	-0.91	3480-9130	18	2400	1.06	LJT+YFOSC
Feb 19	56707.90	13.09	3520-9100	18	2400	1.15	LJT+YFOSC
Feb 25	56713.90	19.09	3500-9100	18	2100	1.21	LJT+YFOSC
Mar 04	56720.72	25.91	3500-9100	18	2500	1.09	LJT+YFOSC
Mar 25	56741.70	46.89	3520-9100	18	2700	1.04	LJT+YFOSC
Apr 10	56757.79	62.98	3530-9150	18	3000	1.25	LJT+YFOSC
Apr 22	56769.76	74.95	3590-9800	50	1500	1.29	LJT+YFOSC
May 17	56794.70	99.89	3920-9680	50	1500	1.32	LJT+YFOSC
May 28	56805.65	110.84	3690-9210	50	1800	1.21	LJT+YFOSC

Note. Spectroscopic observations of SN 2014L.

^a Relative to the V-band maximum, MJD = 56694.81.

(This table is available in machine-readable form.)

Table 4
Absolute Peak Brightness of SN 2014L in *UBVRI* bands

Band	t_{\max} (MJD-56000)	m_{peak} (mag)	M_{peak} (mag)	Δm_{15} (mag)
<i>U</i>	692.45(0.40)	16.45(0.04)	-17.54(0.41)	2.00(0.05)
<i>B</i>	693.16(0.25)	16.16(0.03)	-17.30(0.35)	1.60(0.03)
<i>V</i>	694.81(0.20)	15.06(0.02)	-17.73(0.28)	1.10(0.03)
<i>R</i>	696.88(0.20)	14.54(0.02)	-17.71(0.23)	0.94(0.02)
<i>I</i>	697.33(0.25)	14.14(0.03)	-17.64(0.19)	0.56(0.03)

the $t \sim 26$ day observed spectrum of SN 1994I due to the diffraction fringing effect of the instrument.

It should be noted that the C I $\lambda 9087$ absorption is detected in the spectra of SN 2014L and SN 2007gr. The presence of such carbon line is not necessarily in the $t \sim 26$ day spectrum of SN 1994I due to the diffraction fringing effect of the instrument. However, detection of this C I line was reported in the $t \approx +10$ day spectrum of SN 1994I (Baron et al. 1996). The feature of C I observations indicates that SN 2014L, SN 2007gr, and SN 1994I might arise from carbon-rich progenitors (Baron et al. 1996; Valenti et al. 2008).

4.4. Beginning of Nebular Phase

Figure 7(d) displays the spectra of these SNe at the beginning of nebular phase when the spectra of core-collapse SNe are dominated by a few emissions of IMEs (e.g., O, Mg, Ca). For example, the latest spectrum of SN 2014L is dominated primarily by the emission lines [O I] $\lambda\lambda 6300, 6364$, a blend of [Ca II] $\lambda\lambda 7291, 7324$ and [O II] $\lambda\lambda 7300, 7330$, and the Ca II NIR triplet. However, some photospheric components (e.g., the absorptions of Na I D, O I $\lambda 7774$ and Ca II NIR triplet) are still evident in this phase. Similar features are also found in the spectra of SN 1994I, and SN 2007gr. The BL-Ic SN 1998bw shows similar emissions but contains more photospheric features. It indicates a slower evolution in the broad-lined event.

The spectrum of SN 2012hn at $t \approx +34$ days keeps some photospheric features and dominated by the emissions of [Ca II] $\lambda\lambda 7291, 7324$ and [O II] $\lambda\lambda 7300, 7330$, and the Ca II NIR triplet. Similar emissions are also found in the spectrum of SN 2005E at $t \approx +53$ days with less photospheric components. The difference between Ca-rich event, and SNe Ib/c at the early nebular era is the emission of [O I] $\lambda\lambda 6300, 6364$ which is very weak in the former. Besides, SN 2005E did not develop clear emission of Mg I] and SN 2012hn develops this feature rather slowly. These imply different progenitor systems or explosion mechanism between SNe Ib/c and Ca-rich events. The spectrum of SN 2012hn at $t \approx +151$ days evolved to the later nebular phase is similar to the spectra of SNe Ic at about one year after the explosion. It confirms the fact of fast evolution in Ca-rich events.

The apparent and almost symmetric double-peaked feature is found in the [O I] $\lambda\lambda 6300, 6364$ emissions of SN 2008D. The trace of double-peaked [O I] might exist in that of SN 2007gr and SN 1998bw. However, it is not clear in the spectra of SN 2014L. These might indicate a different geometric structure of the ejecta.

4.5. Velocities

The ejecta velocities derived by the absorption minima of Ca II H&K, Na I D, Si II $\lambda 6355$, C II $\lambda 6580$, O I $\lambda 7774$, Ca II NIR triplet, and C I $\lambda 9087$ of SN 2014L are shown in Figure 9. In the early phase, the Ca II shows a much higher velocity relative to Na I, Si II, C II, and O I, and this discrepancy is similarly seen in type Ia supernovae (i.e., Zhao et al. 2015). This might be due to the fact that Ca II has relatively lower excitation/ionization energy and it can be formed at more distant regions (higher velocities). At $t > +10$ days, the velocities of Ca II, Na I, and O I decline slowly and they all tend to reach a velocity plateau of about 8000–10,000 km s⁻¹. We note that the velocity of Na I D shows a significant increase from 8500 km s⁻¹ to 10000 km s⁻¹ during the period from $t \sim 10$ days to $t \sim 20$ days. This is seen in some SNe Ic (e.g., Hunter et al. 2009) and might be due to the contributions from other spectral lines (e.g., Na II or He I $\lambda 5876$).

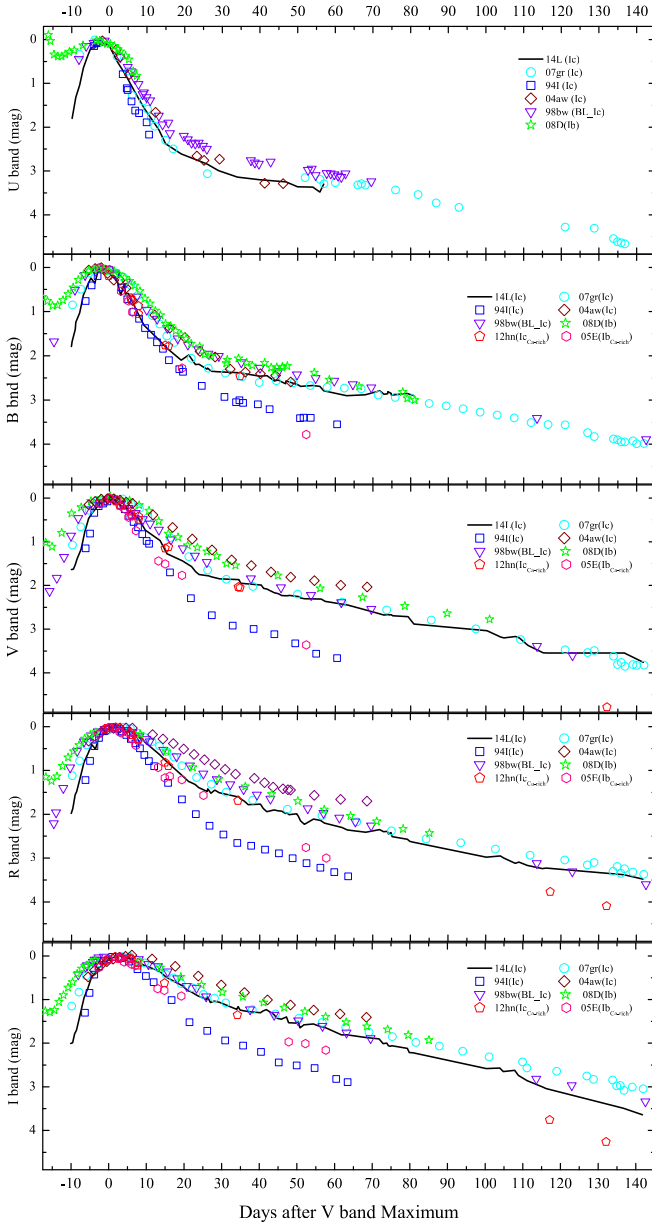


Figure 4. Comparison of the *UBVR* light curves of SN 2014L with some well-observed SNe Ib/c, including SN 2007gr, SN 1994I, SN 2004aw, SN 1998bw, SN 2008D, SN 2012hn, and SN 2005E. All light curves are normalized to their peaks in each band.

Figure 10 shows the comparison of the velocities inferred from Si II $\lambda 6355$ and Ca II NIR triplet for different SNe Ic, including SN 2014L, SN 2007gr, SN 1994I, and SN 2004aw. One can see that SN 2014L shows a higher Si II velocity than that of SN 2007gr. Before the maximum light, the velocity of the Ca II lines in SN 2014L exhibits a remarkably high decline rate $\sim 600 \text{ km s}^{-1} \text{ day}^{-1}$. The more significant decline rate of Ca II velocity makes a lower velocity plateau of SN 2014L than the comparison.

5. Explosion Parameters

Some basic explosion parameters, e.g., synthesized ^{56}Ni mass (M_{Ni}), ejecta mass (M_{ej}), and ejecta kinetic energy (E_{ke}) can be estimated from the observed peak flux (L_{max}) and rise time (t_r) of the bolometric light curve, and the photospheric

velocity (v_{ph}) around the peak brightness with the assumption of a constant opacity. For example, M_{Ni} can be estimated using the Arnett law (Arnett 1982; Stritzinger & Leibundgut 2005):

$$M_{\text{Ni}} = \frac{L_{\text{max}}}{10^{43} \text{ erg s}^{-1}} \times (6.45e^{-\frac{t_r}{\tau_{\text{Ni}}}} + 1.45e^{-\frac{t_r}{\tau_{\text{Co}}}})^{-1}, \quad (1)$$

where, $\tau_{\text{Ni}} = 8.8$ and $\tau_{\text{Co}} = 111.3$ are the decay time of ^{56}Ni and ^{56}Co .

Besides, following Arnett (1982) and the simplifications in WJC 15, we write:

$$M_{\text{ej}} = \frac{1}{2} \frac{\beta c}{\kappa} v_{\text{ph}} t_r^2 = 0.77 M_{\odot} \left(\frac{\kappa}{0.1 \text{ cm}^2 \text{ g}^{-1}} \right)^{-1} v_{\text{ph},9} \left(\frac{t_r}{10 \text{ days}} \right)^2, \quad (2)$$

$$E_{\text{ke}} = \frac{3}{10} M_{\text{ej}} v_{\text{ph}}^2 = \frac{3}{20} \frac{\beta c}{\kappa} v_{\text{ph}}^3 t_r^2 = 4.6 \times 10^{50} \text{ erg} \left(\frac{\kappa}{0.1 \text{ cm}^2 \text{ g}^{-1}} \right)^{-1} v_{\text{ph},9}^3 \left(\frac{t_r}{10 \text{ days}} \right)^2, \quad (3)$$

where κ is the effective optical opacity, $v_{\text{ph},9}$ is the velocity at the photosphere in units of 10^9 cm s^{-1} .

On the other hand, M_{ej} and E_{ke} can be derived from the late-time tail of the light curves,

$$M_{\text{ej}} = \frac{3}{10} \frac{v_{\text{ph}}^2 T_0^2}{C \kappa_{\gamma}}, \quad (4)$$

$$E_{\text{ke}} = \left(\frac{3}{10} \right)^2 \frac{v_{\text{ph}}^4 T_0^2}{C \kappa_{\gamma}}, \quad (5)$$

where C is a dimensionless structure constant, typically about 0.05, κ_{γ} is the gamma-ray opacity, T_0 is the gamma-ray trapping timescale (as defined in Clacchiatti & Wheeler 1996) and can be derived from the observed later-time light curves (see the details in WJC 15).

Explosion parameters of SN 2014L, SN 1994I, and SN 2007gr are measured and compared at below because they show many similarities in observation.

5.1. Rise Time

The rise time t_r is essential to infer the mass of synthesized ^{56}Ni via Equation (1). It can be measured from the very early light curve.

Three groups reported the detection of SN 2014L in their pre-discovery images after the discovery report of Zhang et al. (2014b). The first detection was obtained by Koichi Itagaki (KI) through a 0.5 m reflector telescope at the Takamizawa station on January 24.85 (Yamaoka 2014) in a clear band image (roughly $R = 18.15 \pm 0.50$ mag). Later on, Pan-STARRS1 reported the detection for this SN, marked as PS1-14kd, with the $r = 17.01$ mag on UT 2014 January 26.49. Gregory Haider (GH) also detected it on January 26.54 in the clear images (roughly $R = 17.00 \pm 0.40$ mag) using the 12.5 inches reflector telescope at Christmas Valley. Combining these pre-discovery detections with the early *R*-band light curve obtained by LJT and TNT, the shock breakout date of SN 2014L was derived on 2014 January 22.5 (MJD = 56679.5 \pm 1.0) through the t^2 law approximation of the fireball model, see

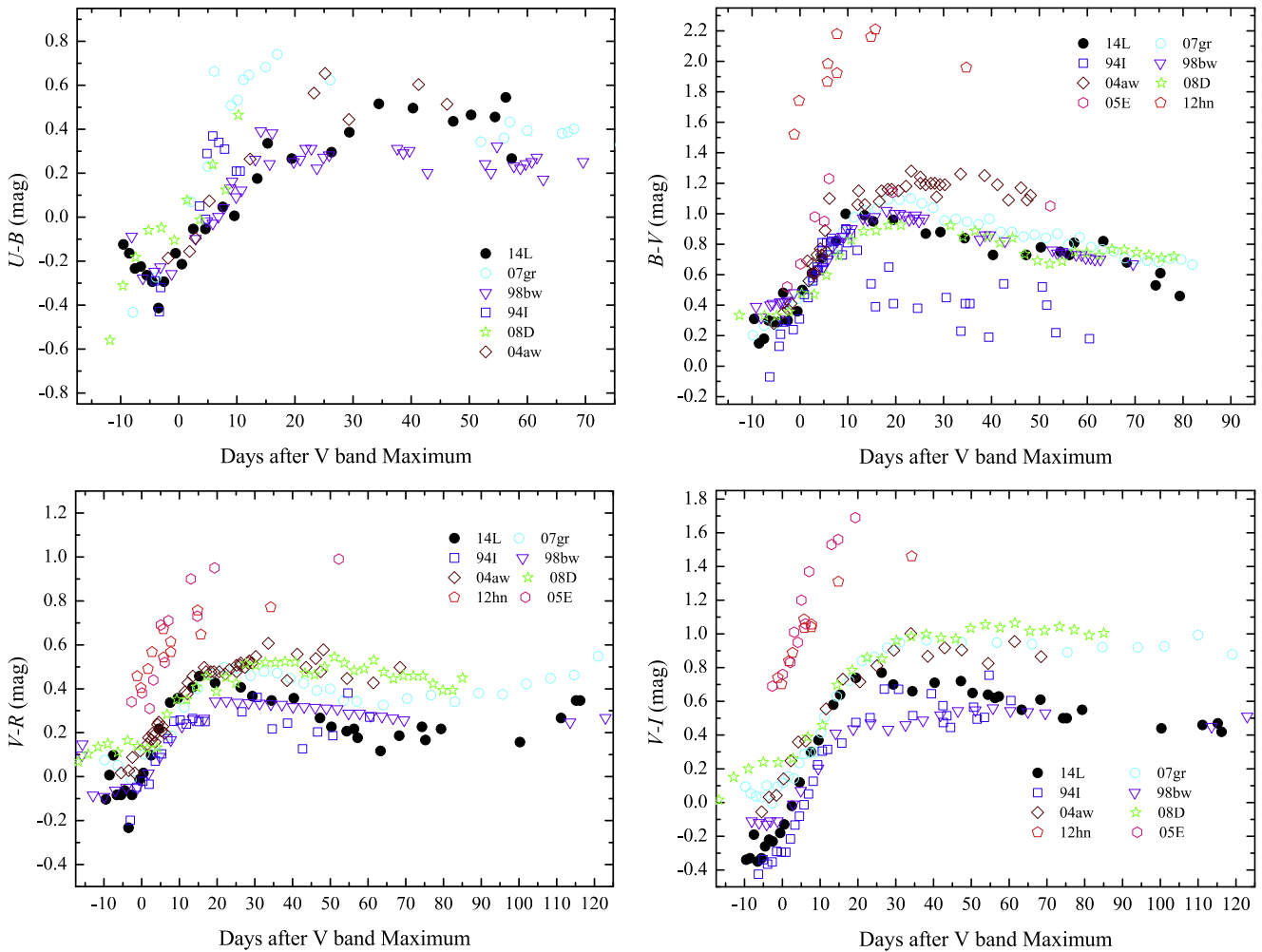


Figure 5. Comparison of the color curves among SN 2014L, SN 2007gr, SN 2012hn, SN 1998bw, SN 2004aw, SN 1994I, and SN 2008D. All of these curves are corrected for the reddening due to the Milky Way and Host galaxies.

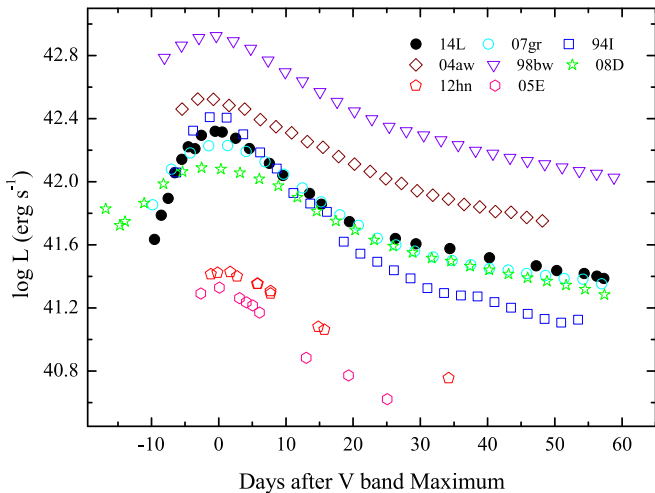


Figure 6. *UBVRi* quasi-bolometric light curves of SN 2014L, SN 2007gr, SN 2005E, SN 2012hn, SN 1998bw, SN 2004aw, SN 1994I, and SN 2008D.

Figure 11. It suggests that SN 2014L reached its bolometric maximum at about 14.5 days after the shock breakout.

However, the fireball model might not be valid in the case of SNe Ic. The physics behind this model is that the increasing internal heating roughly compensates the adiabatic cooling of

the ejecta due to Ni-decay. Since the envelope of SNe Ic is shock-heated, the Ni-decay plays less of a role than in it does in the case of SNe Ia (e.g., SNe Ia mag have 5–10 times more nickel than SNe Ic). Thus, the fireball model may not be capable of giving an accurate prediction for the moment of shock breakout. Furthermore, some poor-fit results of the fireball model in the case of very-young SNe Ia would suggest a steeper power-law index (e.g., Zheng et al. 2013, 2014).

We noted that some previous works (e.g., Valenti et al. 2008; Chen et al. 2014; WJC 15) suggested that the rise time of SN 2007gr is about 13–14 days. Given the narrower light curve of SN 2014L, as presented in Figure 4, its rise time might be shorter than that of the SN 2007gr. Moreover, the light-curve modeling in Section 5.3 suggests $t_r = 13$ days of SN 2014L. Meanwhile, we liberalized the exponent of the power law and found a value of 1.4 with a $t_r = 13$ days. Considering the light-curve comparison of SN 2007gr, the following light-curve modeling, and the result of $t^{1.4}$ fit, we adopted $t_r = 13$ days as the rise time of SN 2014L in the related calculations. The rise time suggests that the shock breakout time of this SN is on 2014 January 24.8 (MJD = 56682.8 ± 1.0). It indicates that the first detection of SN 2014L taken by KI is only a few hours after the shock breakout. Thus, SN 2014L might be the earliest detected SN Ic to date.

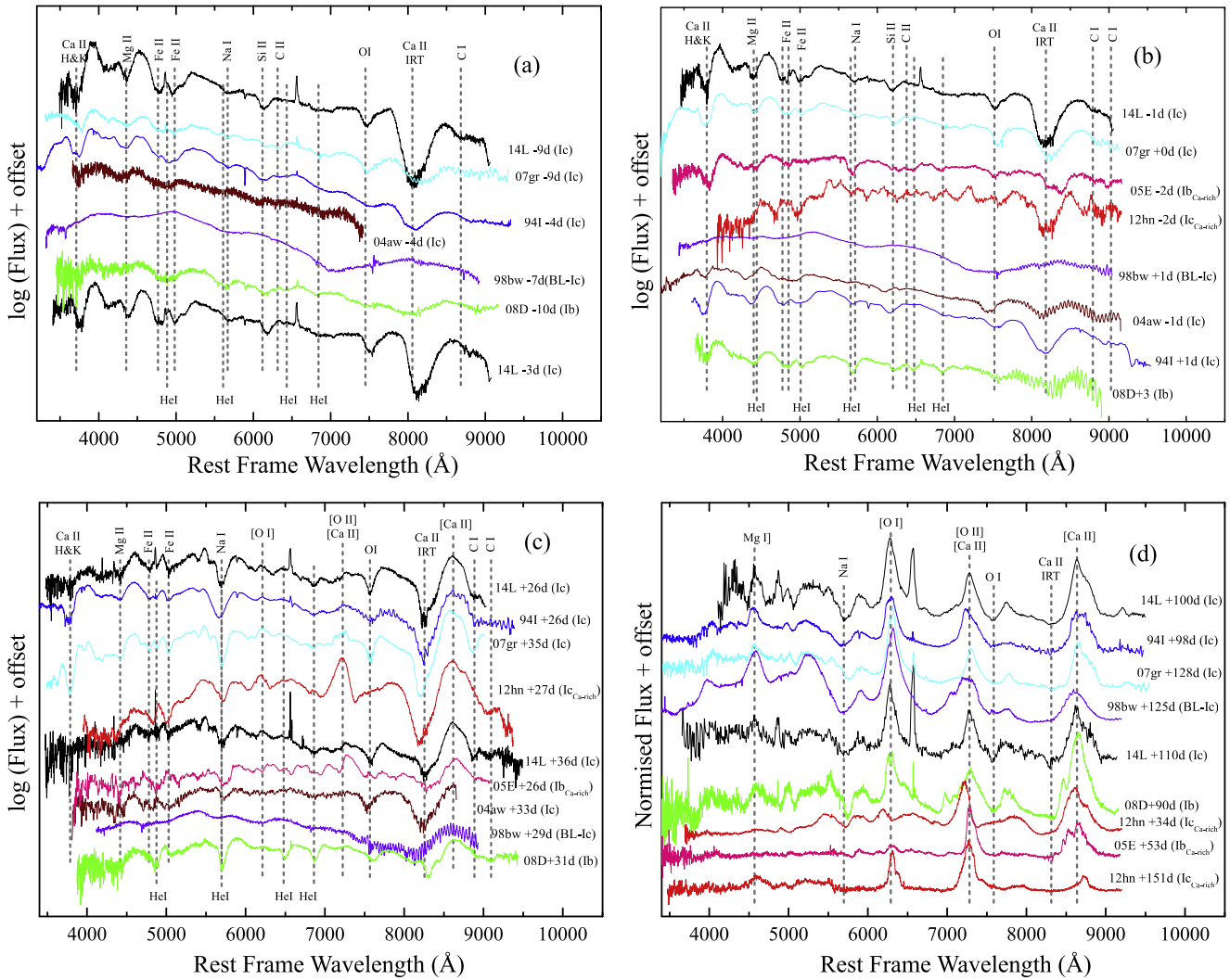


Figure 7. Spectral comparison among SN 2014L, SN 2007gr, SN 2005E, SN 2012hn, SN 1998bw, SN 2004aw, SN 1994I, and SN 2008D at four selected phases. The positions of major line features are marked by dashed-lines referring to the spectral identification of SN 2007gr (Valenti et al. 2008; Hunter et al. 2009; Chen et al. 2014). The spectra in panel (d) are normalized to the flux at around 7300 Å and vertically shifted for better visibility.

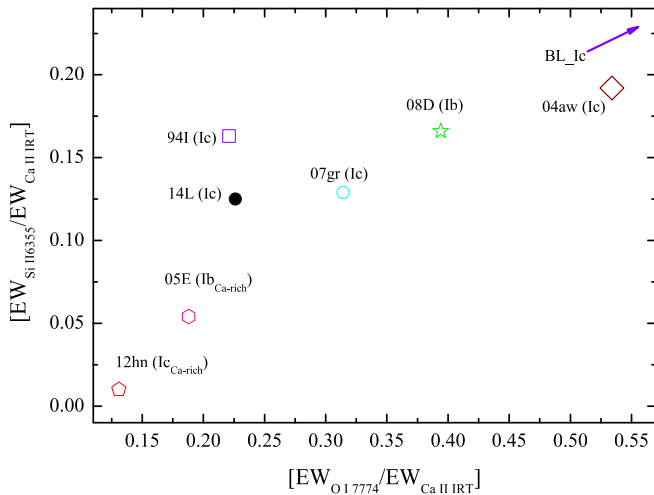


Figure 8. The EW ratio of O I $\lambda 7774$ and Ca II NIR triplet is plotted vs. that of Si II $\lambda 6355$ and Ca II NIR triplet for sample shown in Figure 7. The arrow symbol represents the region expected for SN 1998bw. The size of each symbol is related to the estimated uncertainties.

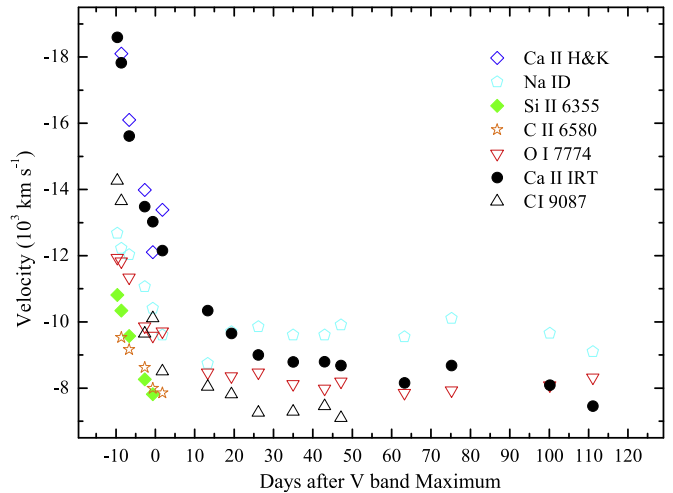


Figure 9. Ejecta velocities of SN 2014L, as inferred from absorption minima of Ca II H&K, Na I D, Si II $\lambda 6355$, C II $\lambda 6580$, O I $\lambda 7774$, Ca II NIR triplet, and C I $\lambda 9087$.

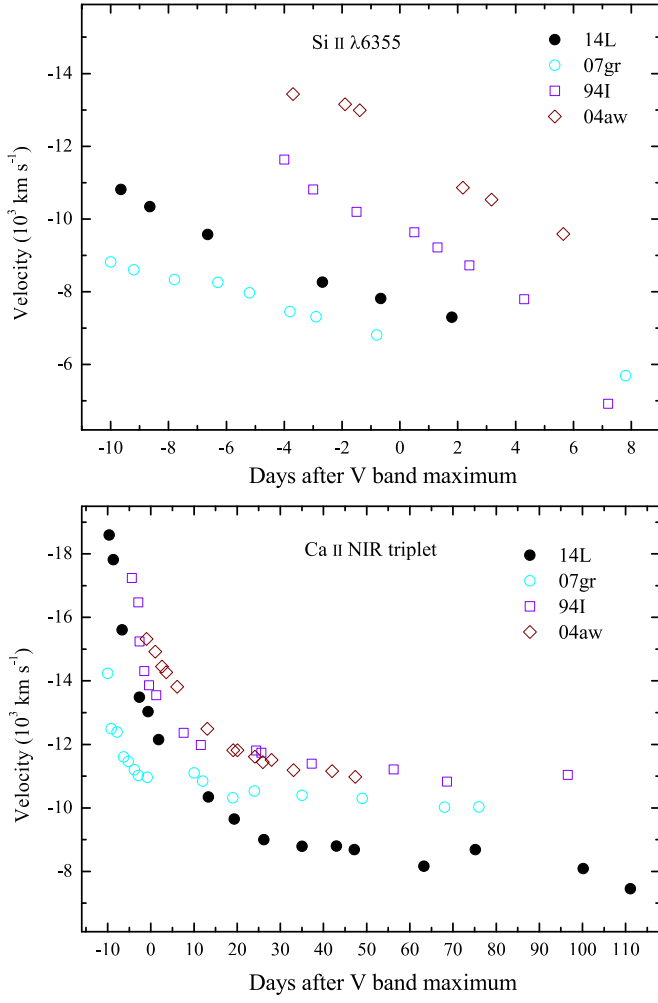


Figure 10. Velocity comparison of SN 2014L, SN 2007gr, SN 1994I, and SN 2004aw. Top panel: velocity inferred from absorption minimum of Si II $\lambda 6355$; Bottom panel: average velocity inferred from absorption minimum of Ca II NIR triplet.

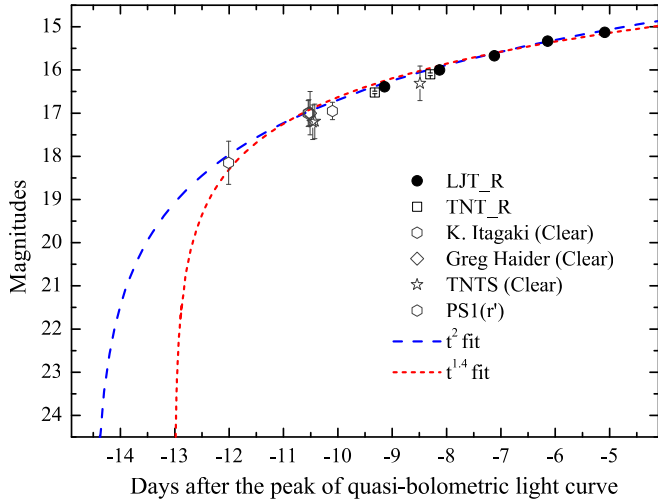


Figure 11. t^n fitting for the early observation of SN 2014L. The exponent of different curves are marked.

5.2. Mass and Energy of the Ejecta

The t_r , L_{\max} , v_{ph} , and T_0 parameters of SN 2014L, SN 1994I, and SN 2007gr derived from the light curve and spectra are

Table 5
Explosion Parameters of Some Well-observed SNe Ic

SN	t_r^a (days)	L_{peak}^b (10^{42} erg s $^{-1}$)	v_{ph} (km s $^{-1}$)	T_0^b (days)	M_{Ni}^{56c} (M_{\odot})
2014L	13.0	2.06	7650	90	0.075
1994I	12.0	2.63	9900	85	0.089
2007gr	14.0	1.72	6700	125	0.066

Notes. Observed parameters of SNe Ic, 1994I, 2014L, and 2007gr. The typical errors for the measurement are 10%–20%.

^a Rise time from the shock breakout to the peak of quasi-bolometric curves in Figure 6.

^b Derived from the light curves at $t > +50$ days.

^c Derived from Equation (1) and the quasi-bolometric curves in Figure 6.

Table 6
Mass and Kinetic Energy of Ejecta

Parameters	14L _p ^a	94I _p ^a	07gr _p ^a	14L _t ^b	94I _t ^b	07gr _t ^b
M_{ej} (M_{\odot})	1.00	1.10	1.01	3.32	5.49	5.26
E_{ke} (foe)	0.35	0.75	0.23	1.16	3.77	1.41

Notes. M_{ej} and E_{ke} of SN 2014L, SN 1994I, and SN 2007gr. The typical errors for the measurement are 15%–25%.

^a Derived from the peak light curves based on Equations (2) and (3) with $\kappa = 0.10$ cm 2 g $^{-1}$.

^b Derived from the tail light curves based on Equations (4) and (5) with $\kappa_{\gamma} = 0.03$ cm 2 g $^{-1}$.

listed in Table 5. A fiducial optical opacity $\kappa = 0.1$ cm 2 g $^{-1}$, and a fiducial gamma-ray opacity $\kappa_{\gamma} = 0.03$ cm 2 g $^{-1}$ are taken to calculate M_{ej} and E_{ke} . In Table 6, as noted by WJC 15, parameters derived from the peak do not match those arising from the tail. That relates to the fiducial value of κ and κ_{γ} adopted in the calculation. If we set the results derived from the peak equal to that from the tail, a relation about κ and κ_{γ} can be written as

$$\begin{aligned} \kappa &= \frac{5}{3} (\beta c) C \frac{\kappa_{\gamma}}{v_{\text{ph}}} \left(\frac{t_r}{T_0} \right)^2 \\ &= 0.01 \text{ cm}^2 \text{ g}^{-1} \frac{\kappa_{\gamma}/0.03 \text{ cm}^2 \text{ g}^{-1}}{v_{\text{ph},9}} \left(\frac{t_{r,10}}{T_{0,100}} \right). \end{aligned} \quad (6)$$

WJC 15 assumed that κ_{γ} is less dependent on explosion parameters than κ . Thus, κ derived from Equation (6), where $\kappa_{\gamma} = 0.03$ cm 2 g $^{-1}$, is close to 0.02–0.03 cm 2 g $^{-1}$. This is much smaller than the assumed $\kappa = 0.1$ cm 2 g $^{-1}$.

5.3. Light-curve Modeling

The bolometric light curve of SN 2014L, SN 1994I, and SN 2007gr have been modeled by applying the LC2.2 code¹³ to check the explosion parameters estimated at above. This code is the most recent version of the LC2 code presented by Nagy & Vinkó (2016). LC2.2 computes the bolometric light curve of a homologous expanding supernova using the radiative diffusion approximation as introduced by Arnett & Fu (1989). The list of model parameters includes the initial radius (R_0), the ejecta mass (M_{ej}), the initial ^{56}Ni mass (M_{Ni}), the total kinetic and thermal energy of the ejecta (E_{ke} and E_{th} ,

¹³ <http://titan.physx.u-szeged.hu/~nagyandi/LC2.2>

Table 7
Parameters of Light-curve Model

Parameters	Model A ^a	Model B ^b	Model C ^c
Parameters for SN 2014L			
$M_{\text{ej}} (M_{\odot})^{\text{d}}$	1.00	3.32	0.83
$E_{\text{ke}}(\text{foe})^{\text{d}}$	0.35	1.16	0.80
$E_{\text{th}}(\text{foe})^{\text{d}}$	1.10	1.10	0.10
$E_{\text{ke}}/E_{\text{th}}$	0.32	1.05	8.00
$\kappa(\text{cm}^2 \text{g}^{-1})^{\text{d}}$	0.10	0.03	0.12
$T_0(\text{days})^{\text{e}}$	55.1	100.5	30.3
$T_+(\text{days})^{\text{e}}$	871.3	1588.9	478.3
$v_{\text{ph}}(\text{km s}^{-1})^{\text{e}}$	7659	7652	12710
Parameters for SN 1994I			
$M_{\text{ej}}(M_{\odot})^{\text{d}}$	1.10	5.49	0.83
$E_{\text{ke}}(\text{foe})^{\text{d}}$	0.75	5.17	1.30
$E_{\text{th}}(\text{foe})^{\text{d}}$	1.20	0.70	0.10
$E_{\text{ke}}/E_{\text{th}}$	0.63	7.39	13.00
$\kappa(\text{cm}^2 \text{g}^{-1})^{\text{d}}$	0.10	0.02	0.14
$T_0(\text{days})^{\text{e}}$	41.4	78.7	23.7
$T_+(\text{days})^{\text{e}}$	654.7	1244.6	375.2
$v_{\text{ph}}(\text{km s}^{-1})^{\text{e}}$	10690	12563	16202
Parameters for SN 2007gr			
$M_{\text{ej}}(M_{\odot})^{\text{d}}$	1.01	5.06	0.78
$E_{\text{ke}}(\text{foe})^{\text{d}}$	0.23	1.17	0.50
$E_{\text{th}}(\text{foe})^{\text{d}}$	0.86	0.85	0.10
$E_{\text{ke}}/E_{\text{th}}$	0.27	1.38	5.00
$\kappa(\text{cm}^2 \text{g}^{-1})^{\text{d}}$	0.10	0.02	0.13
$T_0(\text{days})^{\text{e}}$	68.7	152.5	36.0
$T_+(\text{days})^{\text{e}}$	1085.5	2411.3	568.6
$v_{\text{ph}}(\text{km s}^{-1})^{\text{e}}$	6178	6225	10365

Notes. Model parameters for the synthetic light curves of SN 2014L, SN 1994I, and SN 2007gr. The typical errors for the measurement are 15%–25%.

^a Derived from the peak light curves.

^b Derived from the tail light curves.

^c Best fitting for the light curve at the first full month after shock break.

^d Input parameters of LC2.2 code.

^e Output parameters of LC2.2 code.

respectively), the type and the exponent of the density profile (power-law or exponential), and the average value of the Thompson-scattering opacity (κ) in the envelope.

Recombination of hydrogen and/or helium, which is built-in the code, is not relevant in the case of the Type Ic SNe. Thus, it has been turned off, similar to the additional energy input from magnetar spin-down. LC2.2 assumes fixed gamma-ray and positron opacities, set to their nominal values of $\kappa_{\gamma} = 0.027$ and $\kappa_{+} = 7 \text{ cm}^2 \text{g}^{-1}$, respectively. Thus, they are not adjustable parameters, unlike in the previous version described by Nagy & Vinkó (2016). Note also that while LC2.2, in principle, can model a two-component ejecta having different masses, radii, density profiles, and opacities, we applied only a single component fit to the light curve of these SNe Ic.

The initial radius is not a sensitive parameter in this code. Thus, a constant $R_0 = 4 \times 10^{11} \text{ cm}$ is adopted for the following calculations. Table 7 lists the input parameters of SN 2014L, SN 1994I, and SN 2007gr. M_{Ni} is derived from Equation (1) based on the optical flux because the *UBVRI* bolometric light curves are modeled here. M_{ej} and E_{ke} in Model A and B are derived from the peak (i.e., Equations (2) and (3)) and tail (i.e., Equations (4) and (5)) of the light curves, respectively.

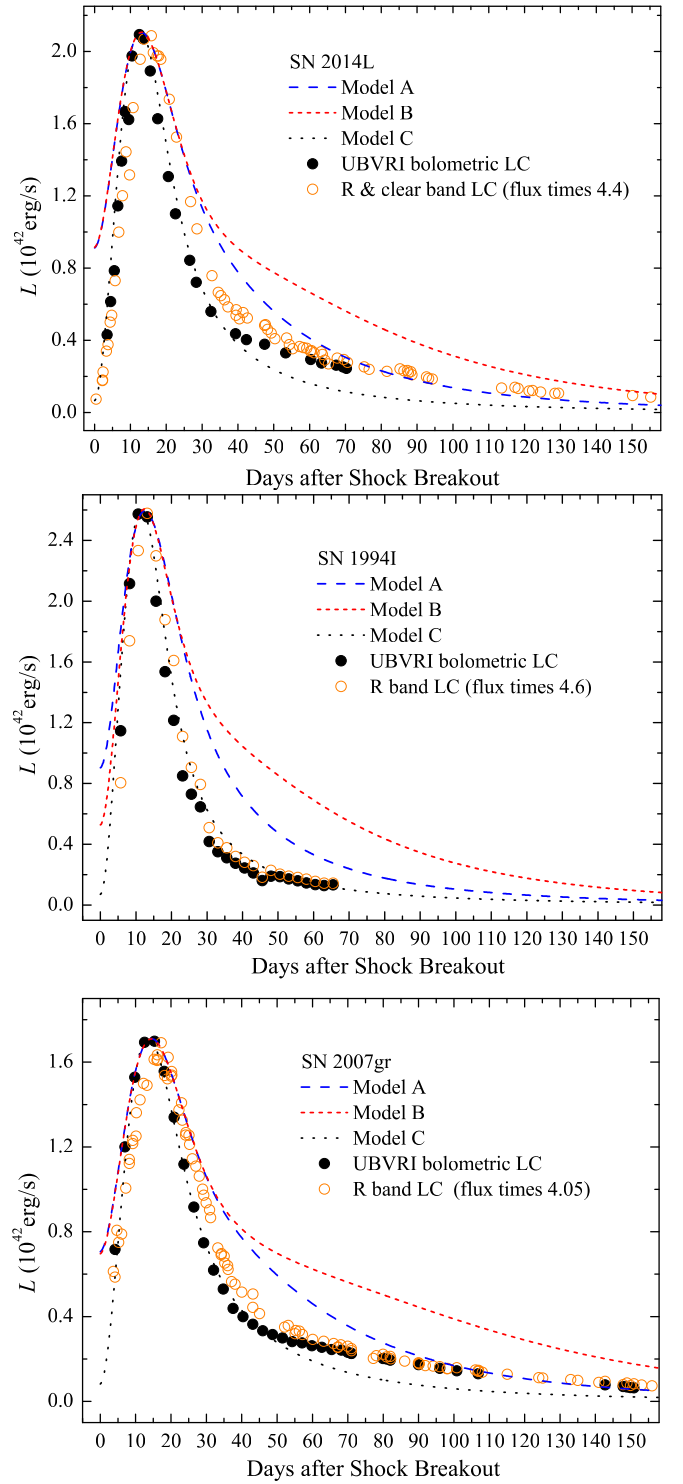


Figure 12. Modeling fitting for the bolometric light curve of SN 2014L, SN 1994I, and SN 2007gr. Only the core of the LC2 model was adopted. The main input parameters are listed in Table 7, see details in the text.

A fiducial optical opacity $\kappa = 0.1 \text{ cm}^2 \text{g}^{-1}$ is adopted in Model A. E_{th} is a free parameter to match the peak between observation and calculation.

Figure 12 displays the modeling results based on the input parameters in Table 7. The *U*- and *B*-band flux are decreased much more quickly than that in the *VRI* bands. Thus, the full *UBVRI* band photometry only covers the first 70 days of SN 2014L. On the other hand, it is reasonable to assume that the

R -band light curve is a good proxy of the bolometric light curve within a constant scaling factor (WJC 15). For comparison, we over-plotted the scaled R -band light curve by assuming the R -band luminosity scales with the bolometric luminosity.

These two models yield a broader light curve than the observation. We noted that the width of light curve produced by LC2.2 code is inversely proportional to the scale of κ and the ratio of E_{ke} and E_{th} . Thus, we liberalized the parameters κ , E_{ke} , and E_{th} , to find a better fit for the observation. In this case, M_{ej} follows κ based on the relation of Equation (2).

The best fitting recorded and plotted as Model C, matches the observations well at $\tau \lesssim 40$ –70 days. For example, Model C gives a good fit for SN 2014L and SN 2007gr at about $\tau \lesssim 40$ –50 days, and the latter curves of the model are fainter than the data. This might be due to the leakage of gamma-rays. The model C of SN 1994I gives a good fit during all of the observational epochs. It is uncertain after $\tau > 70$ days because of the lack of observation. However, the tendency of the observed light curve is to follow the prediction of model C. In brief, model C yields a good fit at $\tau \lesssim 40$ –70 days, and model A gives a good fit for the tail at $\tau > 90$ days. The mismatch between these models is probably due to the oversimplifying assumption of constant opacity. As mentioned before, the rise time derived from model C (i.e., $t_r = 13$ days) is adopted in the above calculation because this model gives proper fitting during the rising phase.

It is remarkable that the ratio of $E_{\text{ke}}/E_{\text{th}}$ in model C is much bigger than that of model A and B. Besides, SN 1994I shows the narrowest light curve in this figure, and it has the highest $E_{\text{ke}}/E_{\text{th}}$ ratio. It seems that the narrower light curve could be the consequence of the faster speed of ejecta. However, this is vigorously challenged by BL SNe Ic, which shows the highest velocity and the broadest light curve. On the other hand, the speeds derived from model C are much higher than those observed, which indicates an overestimation of E_{ke} for these SNe.

6. Summary

We have presented densely sampled photometric and spectroscopic observations of the Type Ic SN 2014L. This SN was likely detected at only a few hours after shock breakout and reached a peak brightness of $L_{\text{max}} = (2.06 \pm 0.50) \times 10^{42} \text{ erg s}^{-1}$ at $\tau \sim 13$ days. The synthesized ^{56}Ni derived from the peak bolometric brightness is $M(\text{Ni}) = 0.075 \pm 0.025 M_{\odot}$. It is noted that some explosion parameters of SN 2014L obtained from the peak brightness mismatch those derived from the tail of the light curve. We leave the issue of the peak/tail conflict for future studies, and only give a range for these parameters for SN 2014L as $M_{\text{ej}} = (1.00\text{--}3.32)M_{\odot}$, $E_{\text{ke}} = (0.35\text{--}1.16) \text{ foe}$, $E_{\text{th}} = 1.10 \text{ foe}$. Nevertheless, the results derived from the light curve around the peak are adopted in the literature more commonly.

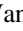

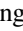
A simple light-curve code was utilized to fit the bolometric light curve, which yields some proper fittings at some individual epochs. The mismatched intervals between observation and modeling might be related to the more complicated behavior of optical opacity of ejecta. This code assumes spherical ejecta, which may not be valid in all SNe Ic. The spherical ejecta assumption may also contribute to the failure of fitting the whole LC, in addition to the issues with the constant κ .

Besides, from the morphological comparison, SN 2014L looks more-or-less similar to SN 2007gr and SN 1994I in both

photometry and spectroscopy. The differences, however, are also remarkable, e.g., the width of the light curve, the strength of Ca II NIR triplet, and the velocity of ejecta. SN 2014L shows a stronger Ca II NIR triplet than SN 2007gr, SN 1994I, and even the Ca-rich events (e.g., SN 2005E, SN 2012hn) during the early phase. However, the ratio of the strengths of O/Ca and Si/Ca in SN 2014L is larger than the Ca-rich events, and it is close to the typical SNe Ic. Thus, the strong Ca II NIR triplet of SN 2014L might suggest the enrichment of IMEs in the outer layer of ejecta. The light-curve width, peak brightness, ejecta velocity, ejecta mass, synthesized ^{56}Ni , and explosive energy of SN 2014L locate between SN 2007gr and SN 1994I. Therefore, the observation of SN 2014L strengthens the physical relation between SN 1994I and SN 2007gr.

We thank the anonymous referee very much for his/her constructive suggestions, which helped to improve the paper a lot. We acknowledge the support of the staff of the Li-Jiang 2.4 m telescope (LJT) and Xing-Long 0.8 m telescope (TNT), 2.16 m telescope (XLT). Funding for the LJT has been provided by the Chinese Academy of Sciences (CAS) and the People's Government of Yunnan Province. The LJT is jointly operated and administrated by Yunnan Observatories and Center for Astronomical Mega-Science, CAS. We also thanks Koichi Itagaki, Greg Haider, and David Bishop for providing the pre-discovery images about this SN. J.Z. is supported by the National Natural Science Foundation of China (NSFC, grants 11403096, 11773067); X.W. is supported by NSFC (grants 11178003, 11325313, and 11633002) and the Major State Basic Research Development Program (2013CB834903); J.V. is supported by GINOP-2.3.2-15-2016-00033 grant of the National Research, Development and Innovation Office (NKFIH) Hungary, funded by the European Union; J.B. is supported by the NSFC (grants 11133006, 11361140347), the Strategic Priority Research Program "The Emergence of Cosmological Structures" of the CAS (grant No. XDB09000000), and the Key Research Program of the CAS (grant No. KJZD-EW-M06); L.C. is supported by the NSFC (grants 11573069). J.M. is supported by the NSFC (grants 11673062) and Hundred Talent Program and the Overseas Talent Program of Yunnan Province; Y.Z. is supported by the NSFC (grants 11661161016); the research of Y. Yang is supported through a Benozio Prize Postdoctoral Fellowship; J.W. is supported by the NSFC (grants 11303085); Y.X. is supported by the NSFC (grants 11573067). This work is also supported by the Western Light Youth Project; Youth Innovation Promotion Association of the CAS (grants 2018081, 2015043, 2018080, 2016054); the Key Laboratory for Research in Galaxies and Cosmology of the CAS; and the Open Project Program of the Key Laboratory of Optical Astronomy, NAOC, CAS.

ORCID iDs

Jujia Zhang  <https://orcid.org/0000-0002-8296-2590>
 Xiaofeng Wang  <https://orcid.org/0000-0002-7334-2357>
 József Vinkó  <https://orcid.org/0000-0001-8764-7832>
 J. Craig Wheeler  <https://orcid.org/0000-0003-1349-6538>
 Tianmeng Zhang  <https://orcid.org/0000-0002-8531-5161>
 Jianguo Wang  <https://orcid.org/0000-0003-4156-3793>
 Jirong Mao  <https://orcid.org/0000-0002-7077-7195>
 Weimin Yi  <https://orcid.org/0000-0001-9314-0552>
 Kaixing Lu  <https://orcid.org/0000-0003-2112-171X>

References

- Akitaya, H., Itoh, R., Moritani, Y., et al. 2014, *CBET*, 3795, 6
- Arnett, W. D. 1982, *ApJ*, 253, 785
- Arnett, W. D., & Fu, A. . 1989, *ApJ*, 340, 396
- Barbon, R., Benetti, S., Rosino, L., et al. 1990, *A&A*, 237, 79
- Baron, E., Hauschildt, P. H., Branch, D., et al. 1996, *MNRAS*, 279, 799
- Bianco, F. B., Modjaz, M., Hicken, M., et al. 2014, *ApJS*, 213, 19
- Branch, D., & Wheeler, J. C. 2017, *Supernova Explosions* (Berlin: Springer)
- Chen, J.-C., Wang, X.-F., Ganeshalingam, M., et al. 2014, *ApJ*, 790, 120
- Childress, M. J., Tucker, B. E., Yuan, F., et al. 2016, *PASA*, 33, 55
- Clocchiatti, A., Suntzeff, N. B., Covarubias, R., & Candia, P. 2011, *AJ*, 141, 163
- Clocchiatti, A., & Wheeler, J. C. 1997, *ApJ*, 491, 375
- Drout, M., Milisavljevic, D., Parrent, J., et al. 2016, *ApJ*, 821, 57
- Drout, M., Soderberg, A. M., Gal-Yam, A., et al. 2011, *ApJ*, 741, 97
- Fan, Y.-F., Bai, J.-M., Zhang, J.-J., et al. 2015, *RAA*, 15, 918
- Filippenko, A. V. 1997, *ARA&A*, 35, 309
- Filippenko, A. V., Barth, A. J., Matheson, T., et al. 1995, *ApJ*, 450, L11s
- Galama, T. J., Vreeswijk, P. M., van Paradijs, J., et al. 1998, *Natur*, 395, 670
- Hachisu, I., Matsuda, T., Nomoto, K., & Shigeyama, T. 1991, *ApJ*, 368, L27
- Hjorth, J., Sollerman, J., Moller, P., et al. 2003, *Natur*, 423, 6942
- Houck, J., & Fransson, C. 1996, *ApJ*, 456, 811
- Huang, F., Li, J. Z., Wang, X. F., et al. 2012, *RAA*, 11, 1585
- Hunter, D. J., Valenti, S., Kotak, R., et al. 2009, *A&A*, 508, 371
- Iwamoto, K., Mazzali, P. A., Nomoto, K., et al. 1998, *Natur*, 395, 672
- Kasliwal, M. M., Kulkarni, S. R., Gal-Yam, A., et al. 2012, *ApJ*, 755, 161
- Landolt, A. V. 1992, *AJ*, 104, 340
- Li, W.-X., Sai, H.-N., Wang, X.-F., & Zhang, T.-M. 2014, *CBET*, 3795, 3
- Liu, Y.-Q., Modjaz, M., Bianco, F. B., & Graur, O. 2016, *ApJ*, 827, 90
- Mazzali, P. A., Deng, J., Tominaga, N., et al. 2003, *ApJ*, 599, L95
- Milisavljevic, D., Margutti, R., Parrent, J. T., et al. 2015, *ApJ*, 799, 51
- Modjaz, M., Blondin, S., Kirshner, R. P., et al. 2014, *AJ*, 147, 99
- Modjaz, M., Li, W., Butler, N., et al. 2009, *ApJ*, 702, 226
- Nagy, A., & Vinkó, J. 2016, *A&A*, 589, 53
- Ochner, P., Benetti, S., Pastorello, A., et al. 2014, *CBET*, 3795, 5
- Patat, F., Cappellaro, E., Danziger, J., et al. 2001, *ApJ*, 500, 900
- Perets, H. B., Gal-Yam, A., Mazzali, P. A., et al. 2010, *Natur*, 465, 322
- Phillips, M., Simon, J., Morrell, N., et al. 2013, *ApJ*, 779, 38
- Poznanski, D., Butler, N., Filippenko, A. V., et al. 2009, *ApJ*, 694, 1067
- Poznanski, D., Ganeshalingam, M., Silverman, J. M., & Filippenko, A. V. 2011, *MNRAS*, 415, L81
- Richmo, M. W., Van Dyk, S. D., Ho, W., et al. 1996, *AJ*, 111, 327
- Schlafly, E. F., & Finkbeiner, D. P. 2011, *ApJ*, 737, 103
- Shigeyama, T., Nomoto, K., Tsujimoto, T., & Hash, M. 1990, *ApJ*, 361, L23
- Soria, R., & Wong, D. S. 2016, *MNRAS*, 372, 1531
- Stritzinger, M., & Leibundgut, B. 2005, *A&A*, 431, 423
- Tanaka, M., Yamanaka, M., Maeda, K., et al. 2009, *ApJ*, 700, 1680
- Taubenberger, S., Pastorello, A., Mazzali, P. A., et al. 2006, *MNRAS*, 371, 1459
- Tully, R. B., Courtois, H. M., Dolphin, A. E., et al. 2013, *AJ*, 146, 86
- Turatto, M., Benetti, S., & Cappellaro, E. 2003, in *From Twilight to Highlight: The Physics of Supernovae*, ed. W. Hillebrandt & B. Leibundgut (Berlin: Springer), 200
- Valenti, S., Elias-Rosa, N., Taubenberger, S., et al. 2008, *ApJ*, 673, 155
- Valenti, S., Yuan, F., Taubenberger, S., et al. 2014, *MNRAS*, 437, 1519
- Wang, X., Li, W., Filippenko, A. V., et al. 2008, *ApJ*, 675, 626
- Wheeler, J. C., Harkness, R. P., Barker, E. S., et al. 1987, *ApJ*, 313, L69
- Wheeler, J. C., Harkness, R. P., Clocchiatti, A., et al. 1994, *ApJ*, 436, L135
- Wheeler, J. C., Johnson, V., & Clocchiatti, A. 2015, *MNRAS*, 450, 1295, (WJC 15)
- Woosley, S. E., & Bloom, J. S. 2006, *ARA&A*, 44, 507
- Woosley, S. E., Langer, N., & Weaver, T. A. 1993, *ApJ*, 411, 823
- Yamaoka, H. 2014, *CBET*, 3795, 2
- Zhang, J.-J., & Wang, X.-F. 2014, *CBET*, 3795, 4
- Zhang, J.-J., Wang, X.-F., Bai, J.-M., et al. 2014a, *AJ*, 148, 1
- Zhang, T.-M., Wang, X.-F., Chen, J.-C., et al. 2015, *RAA*, 15, 215
- Zhang, T.-M., Wang, X.-F., Mo, J., & Chen, J.-C. 2014b, *CBET*, 3795, 1
- Zhao, X.-L., Wang, X.-F., Maeda, K., et al. 2015, *ApJS*, 220, 20
- Zheng, W.-K., Shivvers, I., Filippenko, A. V., et al. 2014, *ApJL*, 783, 24
- Zheng, W.-K., Silverman, J. M., Filippenko, A. V., et al. 2013, *ApJL*, 778, 15